

Hypercube States for Sub-Planck Sensing

L. A. Howard¹, T. J. Weinhold¹, J. Combes¹, F. Shahandeh², M. R. Vanner³, M. Ringbauer⁴, and A. G. White¹

¹Centre for Engineered Quantum Systems, School of Mathematics and Physics, University of Queensland, Brisbane, Australia.

²Department of Physics, Swansea University, United Kingdom.

³QOLS, Blackett Laboratory, Imperial College London, London, United Kingdom.

⁴Institute for Experimental Physics, University of Innsbruck, Innsbruck, Austria.

We introduce hypercube states, a class of continuous-variable quantum states generated as orthographic projections of hypercubes in phase space. Hypercube states exhibit phase-space features much smaller than Planck's constant, making them sensitive to perturbations at extremely small scales. We show that the sensitivity of these states is surprisingly robust, making them a practical resource for sensing applications. In a high-temperature proof-of-principle experiment we observe, and match to theory, the signature outer-edge vertex structure of hypercube states.

Over recent years quantum-enhanced sensors have proven their potential to break classical sensitivity limits and transform the landscape of sensing technology [1]. Of particular interest in this context is the sensing of weak forces with applications from accelerometers to fundamental tests of gravity [2].

For a quantum system to make a good sensor, it is crucial that the state of the system after the action of a small force is as distinguishable as possible from the initial state. This desirable property is closely related to the size of the smallest features in the quantum state's phase space representation [3]. Roughly speaking, two quantum states with smallest features occupying an area on the order of d , can become maximally distinguishable for displacements on the order of \sqrt{d} . Similarly, the rate of change in distinguishability in response to a displacement—a measure of the sensor's sensitivity—is a function of the size of the state's phase-space features. Quantum mechanics generally limits the size of these features to be at least on the order of \hbar , which is variously known as the shot-noise or standard quantum limit depending on the area of physics in which it arises.

Yet, quantum theory also provides a way around this limit, and states such as the Schrödinger-cat state [4]—and the more-recently introduced compass state [3, 5]—show features at a scale below \hbar . States with such *sub-Planck* features have thus attracted significant theoretical attention [5–11] for their potential in sensing applications. However, most of the theory to date has focused on pure states, leaving open the question of how sensitive sub-Planck states will be under realistic conditions.

Here we introduce and study in detail a class of non-classical states that we call *hypercube states*. These states are obtained as Petrie-polygon orthographic projections of n -cubes [12], see Fig. 1, into phase space, where the polygon vertices correspond to the location of coherent states, and interference fringes are observed between every pair of vertices, see Fig. 2. Our class of states in particular includes the Schrödinger-cat state and the compass state as the lowest-order special cases, and all hypercube states exhibit sub-Planck phase-space features that decrease in size with the order of the state, making them an attractive resource for quantum metrology. We

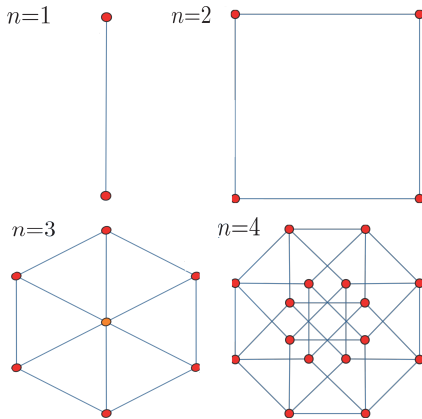


FIG. 1. Petrie polygon orthographic projections of first four n -cubes. Red dots represents the projection of a single vertex onto a unique point in phase space, and orange dots the projection of two vertices onto the same point. $n=1$ is the projection of a line-segment; $n=2$ of a square; $n=3$ of a cube; and $n=4$ of a tesseract.

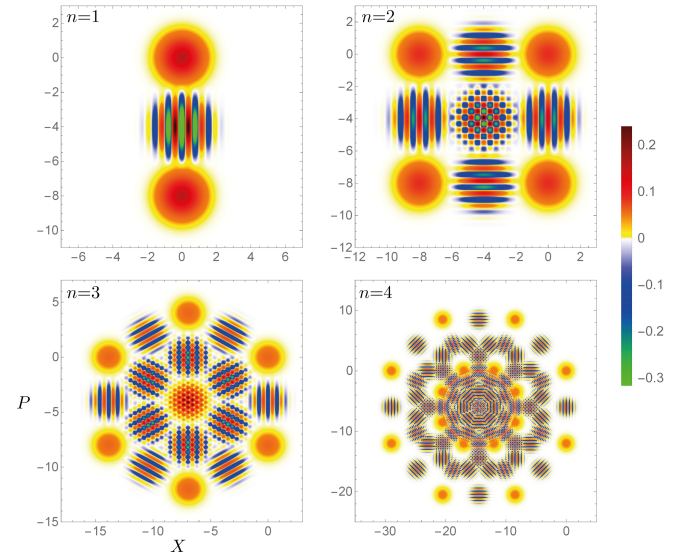


FIG. 2. Density plots of the Wigner functions of the first four hypercube states: $n=1$ Schrödinger-cat state; $n=2$ compass state; $n=3$ cube state; $n=4$ tesseract state

show how to produce hypercube states in mechanical resonators, using multiple applications of a recently developed optomechanical technique [13] that is applicable to a wide range of state-of-the-art experiments. We analyse the so produced hypercube states in different regimes of temperature and interaction strength, which determines the distance between the coherent states at the vertices of the hypercubes. Moreover, we experimentally observe the signature of the square, cube, and tesseract states that survives in the high temperature regime. Specifically, we show that hypercube states become progressively more sensitive as their order increases and that this sensitivity is robust to variations in temperature and/or interaction strength of the state.

In the technique introduced in Ref. [13], the detection of a single photon heralds the successful application of the measurement operator $\Upsilon = e^{-|\alpha|^2} \alpha (\mathcal{D}(-i\mu/\sqrt{2}) - 1)/\sqrt{2}$ to the mechanical resonator. Here α is the amplitude of the weak coherent state with wavelength λ , that mediates the displacement, and $\mathcal{D}(-i\mu/\sqrt{2})$ is the displacement operator for a momentum displacement by $\mu/\sqrt{2}$, where $\mu = 4\pi x_0/\lambda$ is the interaction strength (which is equivalent to the optomechanical coupling strength in an optomechanical setting), and $x_0 = \sqrt{\hbar/m\omega}$ is the zero-point fluctuation of the mechanical resonator with frequency ω and effective mass m [13], see Supplementary Material (SM) for details. The resonator is thus left in a superposition of the original state and being displaced by $\mu/\sqrt{2}$.

Mechanical hypercube states can now be generated by a sequence of applications of Υ , with intermittent free evolution of the mechanics for a duration $t = T/2n$, where T is the period of the mechanical oscillator. In phase space this is described by the operator

$$\mathcal{Y}_n \propto \prod_{i=1}^n (R(\pi/n) \Upsilon), \quad (1)$$

where $R(\theta)$ corresponds to a phase-space rotation due to the mechanical free evolution with $\theta = t/T \times 2\pi$, see SM for details. The ideal phase-space representation in terms of the Wigner quasiprobability distribution [4] of the lowest order lowest order hypercube states resulting from this method are shown in Fig. 2.

We now investigate theoretically the sensitivity of these hypercube states in three limiting regimes defined by the interaction strength, μ , and temperature of the mechanical mode, as measured by the average phonon number \bar{n} . The three regimes are: (i) *cold, large-coupling*: mechanical resonator in the ground state, $\bar{n}=0$, and $\mu=6, 8$, and 12 , for the second-, third-, and fourth- order hypercube states respectively; (ii) *cold, small-coupling*: mechanical resonator in the ground state, $\bar{n}=0$, and $\mu=8 \times 10^{-9}$; and (iii) *hot, small-coupling*: our experimental regime of a high temperature mechanical resonator, $\bar{n} \sim 10^{15}$, and small interaction, $\mu=8 \times 10^{-9}$. To quantify a state's sensitivity to a displacement of σ , we consider the

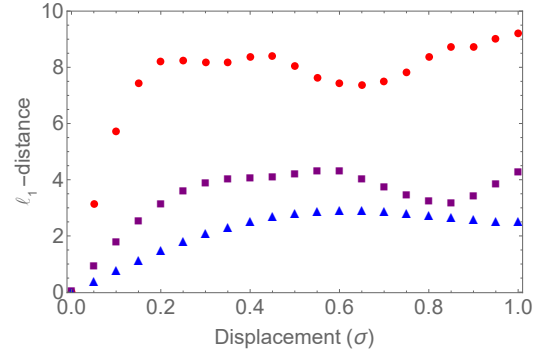


FIG. 3. The ℓ_1 -distance between displaced and undisplaced hypercube states in the momentum quadrature, in terms of the mechanical ground-state width σ . Hypercube states shown are: compass ($n=2$, blue triangles); cube ($n=3$, magenta squares); and tesseract ($n=4$, red circles). For small displacements, $0 < \sigma \lesssim 0.1$, the gradient of the ℓ_1 -distance indicates that hypercube states are sensitive—increasingly so with order n —to small perturbations.

ℓ_1 -distance between the normalised Wigner functions of the initial state W_ρ , and the displaced version of it W_{ρ_σ} defined as,

$$\|W_{\rho_\sigma} - W_\rho\|_1 = \int_{-\infty}^{\infty} \int_{-\infty}^{\infty} dx dp |W_{\rho_\sigma}(x, p) - W_\rho(x, p)|.$$

The sensitivity of the state to displacement is then the rate of change of the ℓ_1 -distance, $d\ell_1/d\sigma$. This quantity is a heuristic for how quickly a displaced state becomes distinguishable from the original and can easily be applied in the thermal regime, a key requirement of this work.

Figure 4 shows density plots of the Wigner functions of second-order hypercube states created in our scheme as they transition between the three limiting regimes introduced above. The figure serves to provide a visual guide to the sensitivity results shown in Fig. 5, and gives context to our experimental results, by showing how the features evolve as we move from the ideal large-coupling ground state regime to more experimentally realistic regimes, and eventually to the hot small-coupling regime used in our experiment.

The numerically evaluated ℓ_1 -distance of the second-, third- and fourth-order hypercube states under momentum displacement is shown in Fig. 3. For small perturbations in the range, $0 < \sigma < 0.1$, the gradient, $d\ell_1/d\sigma$, increases sharply with the order of the hypercube states, highlighting the potential of hypercube states for sensing small displacements.

Figure 4 contains a number of important observations. The top row of Fig. 4 shows that in the cold regime, decreasing the coupling strength leads to larger phase-space features and thus lower sensitivity, as shown in Fig. 5a. Note, however, that the sensitivity to position or momentum displacement remains above that of a coherent state for all values of μ . Note that as the interaction strength

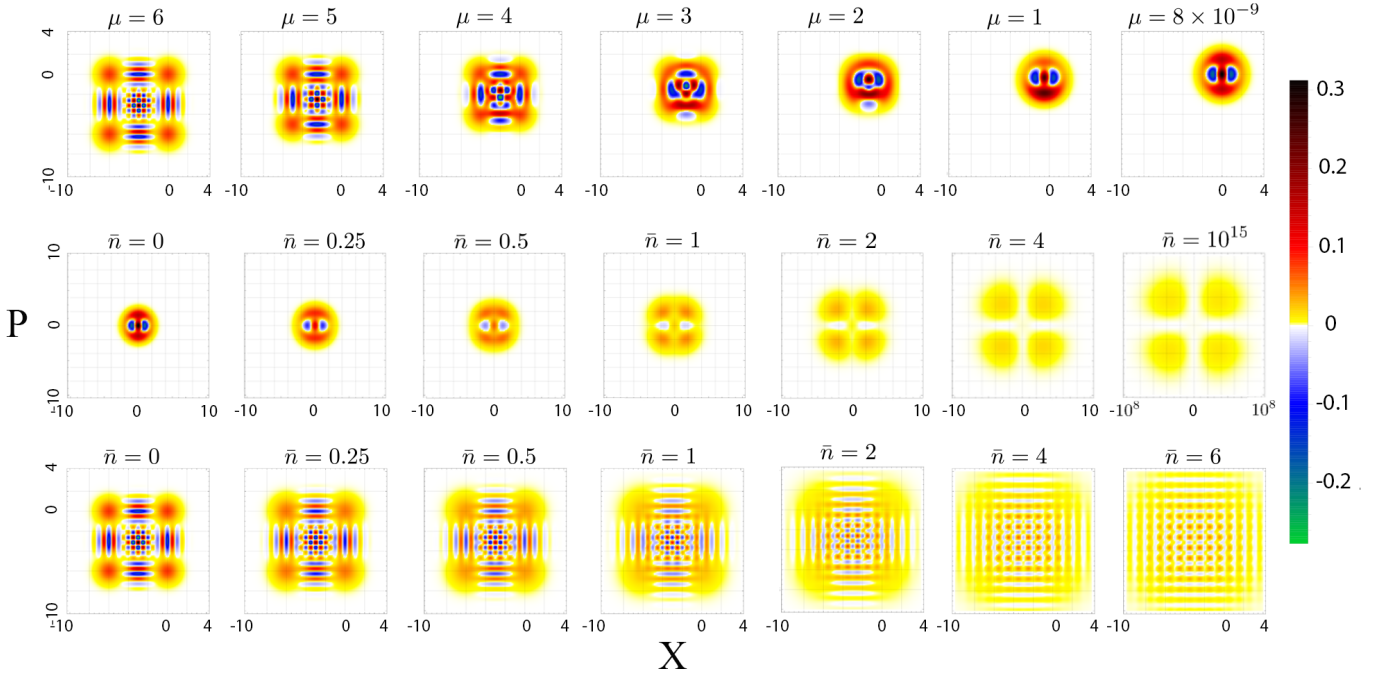


FIG. 4. Theoretical density plots of the Wigner function in position-momentum (X - P) phase space, for a mechanical resonator in the $n=2$ hypercube state—compass state—produced by our scheme. The colour bar on right shows the value of the Wigner function where blue and green indicate areas of negative quasiprobability. **Top row.** Cold temperature: large \rightarrow small coupling ($\bar{n}=0$; $\mu=6 \rightarrow \mu=8 \times 10^{-9}$). **Middle row** Small coupling: cold \rightarrow hot temperature ($\mu=8 \times 10^{-9}$; $\bar{n}=0 \rightarrow \bar{n}=10^{15}$; the colours in the last panel are scaled by 10^8 in accordance with the axis scaling). **Bottom row** Large coupling: cold \rightarrow warm temperature ($\mu=6$; $\bar{n}=0 \rightarrow \bar{n}=6$).

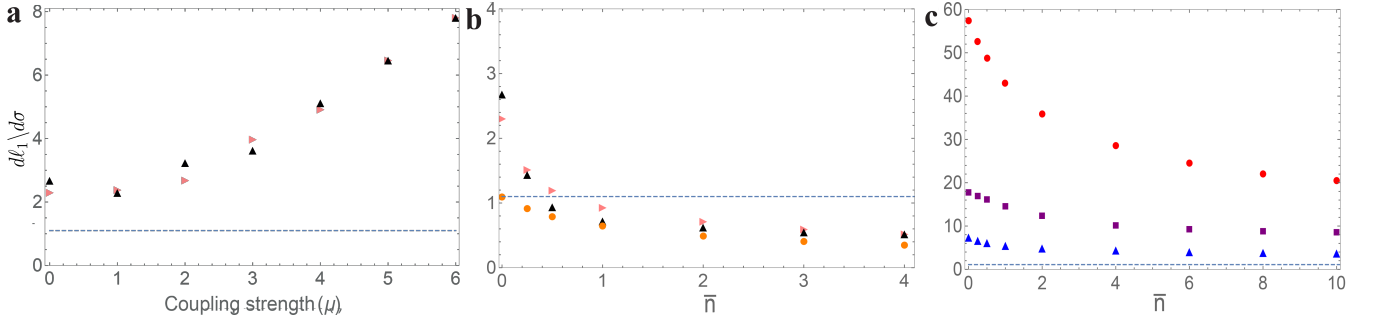


FIG. 5. The sensitivity, $d\ell_1/d\sigma$, of the ℓ_1 -distance for displacements in position (pink horizontal triangles) / momentum (black vertical triangles) for the second-order hypercube states. Coherent-state sensitivity at zero temperature, \bar{n} , is shown by a blue dashed line. **a)** Top row of Fig. 4 ($\bar{n}=0$; $\mu=6 \rightarrow \mu=8 \times 10^{-9}$). Hypercube states are more sensitive than coherent states for all values of μ . **b)** Middle row of Fig. 4 ($\mu=8 \times 10^{-9}$; $\bar{n}=0 \rightarrow \bar{n}=4$). Hypercube states are more sensitive than coherent states in the same thermal regime (orange circles), and for values of $\bar{n} \lesssim 0.25$ are more sensitive than even the zero-temperature coherent state. **c)** Bottom row of Fig. 4 ($\mu=6, 8, 12$; $\bar{n}=0 \rightarrow \bar{n}=10$). Sensitivity for displacements in momentum (or equally position) for second- (blue triangles, $\mu=6$), third- (magenta squares, $\mu=8$) and fourth- (red dots, $\mu=12$) order hypercube states. Hypercube states are more sensitive than even zero-temperature coherent states for a wide range of experimental parameters; note the increase in sensitivity with the order of the hypercube state. A similar plot, S3, where μ is constant for all three orders of hypercube state is shown in the SM to further highlight that sensitivity increases with hypercube order.

decreases, we see the symmetry around the position axis break: at some values the state is more sensitive to displacements in momentum than in position; at other values the opposite is true, see SM for details.

The middle row of Fig. 4 shows that, as the temperature increases in the small coupling regime, we see Wigner negativity and smaller scale features disappear as the outer-vertex-structure—observed in our experi-

mental results—becomes the dominant feature. Note that, despite the small coupling, the hypercube states are more sensitive than coherent states for the same average phonon number, \bar{n} , see Fig. 5b. For phonon numbers between 0 and $\lesssim 0.25$ the hypercube states are more sensitive than a coherent state at zero temperature.

The bottom row of Fig. 4 shows that in the strong coupling regime, periodic and symmetric sub-Planck fea-

tures are visible for $0 < \bar{n} < 6$, and indeed exist even at much higher temperatures. A detailed study of the limits of this sub-Planck structure as \bar{n} increases remains an open question. Figure 5c highlights that this implies robust sensitivity which increases with the order of the hypercube. These results apply equally to displacements along the position or momentum axis.

We experimentally implemented our scheme in the hot small-coupling regime using the apparatus from Ref. [13] with a 100 ng ($\simeq 10^{16}$ atoms) mechanical resonator. To ensure a large physical displacement that can be easily measured, the resonator is driven with a piezo (in order to create a Gaussian state in phase space the piezo drive voltage is Chi-distributed due to the drive voltage coupling to $\sqrt{X^2 + P^2}$). This gives the resonator an effective temperature of $\bar{n} = 10^{15}$. The mechanical resonator was coupled to 795 nm light, with the application of the measurement operator \mathcal{Y}_n heralded by n sequential single-photon detections.

Detection of photons separated by $T/2n$, where T is the mechanical period, was accomplished by splitting the electronic signal from the photon detector into multiple paths of varying lengths and then looking for coincidences between the paths. For example, to detect creation of the $n=2$ hypercube state, we split the signal into two logical paths, one of which takes time $T/4$ longer for the signal to traverse. Two photons separated by $T/4$ will then create a coincidence event. This coincidence event triggers the recording of a time trace of the mechanical position via homodyne measurement, which can be used to reconstruct the phase space position of the mechanical resonator (see SM for details).

Detection of the third- and fourth- order hypercube states requires conditioning on three and four photons, respectively, which requires splitting the signal into three and four logical paths respectively. The specific timing between photons for the second, third, and fourth order hypercube states was $(2.36\mu\text{s})$, $(1.57\mu\text{s}, 1.57\mu\text{s})$, and, $(1.24\mu\text{s}, 1.12\mu\text{s}, 1.18\mu\text{s})$, respectively. (The timing was not equal for the fourth-order hypercube state due to cabling limitations).

The top row of Fig. 6 shows the ideal results expected in the hot small-coupling regime: probability densities that reproduce the outer-ring of vertices of the Petrie projections in Fig. 1, and that do not contain quantum features, or sub-Planck structure—as expected due to the high temperature. These plots are generated by applying \mathcal{Y}_n of equation 1.

There are several common technical limitations affecting our experiment: drift in the interferometer setting, ϕ ; experimental timing uncertainties when applying $R(\pi/2n)$; and variations from the mean due to counting statistics. We constructed a model to account for these limitations, the predictions of which are shown in the middle row of Fig. 6, with notable variations in the height, width, and shape of the peaks in the probability

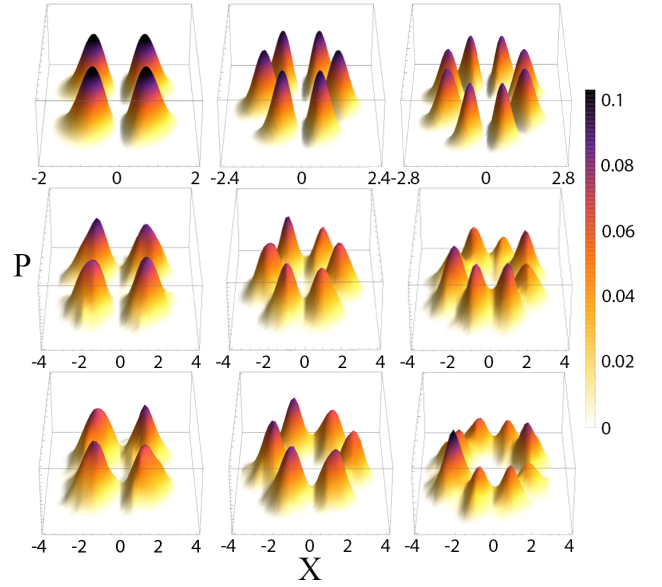


FIG. 6. Normalised probability densities of hypercube states; left to right columns correspond to second-, third- and fourth-order hypercube states. **Top row.** Ideal densities, from equation 1: populations match the outer-ring of vertices of the Petrie projections in Fig. 1; quantum features such as sub-Planck structure are absent due to high temperature. **Middle row.** Densities predicted from a model which accounts for experimental drift, timing uncertainties and counting statistics (see supplementary section). Note the predicted variations in peak height, width and shape. **Bottom row.** Measured probability densities: note the good match to the model in peak variations. The signature of hypercube states in the thermal regime—the ring of outer-edge-vertices—is clearly visible. All axes are in units of $\lambda_R/4 = 158.2\text{nm}$, see SM for details.

densities; see Supplementary Materials for details. The bottom row shows our measured results which, which show the same features: there is excellent agreement between the model predictions and our experiments.

The discovery of this new class of quantum states, and modelling their utility for sensing over a surprisingly large range of experimental parameters, was driven by the search for robust quantum sensors. Future improvement to our experimental scheme include moving into the cold experimental regime, investigating methods to minimise losses due to mechanical damping, and developing operational schemes to extract the fidelity or ℓ_1 -distance. Achieving this will require an amalgamation of current technologies for measurement at the sub-Planck scale [14], and cooling a mechanical resonator to close to the ground state; an amalgamation that already exists in several forms today [15, 16]. Creation of hypercube states within a mechanical resonator, or otherwise, will open up avenues for experimental applications requiring extremely high sensitivity, such as tests of quantum gravity theories [17], gravity-induced decoherence [18], and of quantum theory at the macroscopic scale [19].

Acknowledgements. We acknowledge support from:

the Australian Research Council (ARC) via the Centre of Excellence for Engineered Quantum Systems (EQUS, CE170100009), a Discovery Project for MRV (DP140101638) and a Discovery Early Career Researcher Award for JC (DE160100356); the Engineering and Physical Sciences Research Council (EP/N014995/1); and the University of Queensland by a Vice-Chancellor's Senior Research and Teaching Fellowship for AGW. We acknowledge the traditional owners of the land on which the University of Queensland is situated, the Turrbal and Jagera people.

-
- [1] I. Favero and F. Marquardt, *Focus on optomechanics*, [New J. Phys.](#) **16**, 085006 (2014).
 - [2] M. Aspelmeyer, T. J. Kippenberg, and F. Marquardt, *Cavity optomechanics*, [Rev. Mod. Phys.](#) **86**, 1391 (2014), [arXiv:0712.1618](#).
 - [3] W. H. Zurek, *Sub-planck structure in phase space and its relevance for quantum decoherence*, [Nature](#) **412**, 712 EP (2001).
 - [4] U. Leonhardt, *Measuring the quantum state of light*, Cambridge studies in modern optics (Cambridge University Press, New York, 1997).
 - [5] F. Toscano, D. A. R. Dalvit, L. Davidovich, and W. H. Zurek, *Sub-planck phase-space structures and heisenberg-limited measurements*, [Phys. Rev. A](#) **73**, 023803 (2006).
 - [6] G. S. Agarwal and P. K. Pathak, *Mesoscopic superposition of states with sub-planck structures in phase space*, [Phys. Rev. A](#) **70**, 053813 (2004).
 - [7] D. A. R. Dalvit, R. L. de Matos Filho, and F. Toscano, *Quantum metrology at the heisenberg limit with ion trap motional compass states*, [New J. Phys.](#) **8**, 276 (2006).
 - [8] S. Ghosh, A. Chiruvelli, J. Banerji, and P. K. Panigrahi, *Mesoscopic superposition and sub-planck-scale structure in molecular wave packets*, [Phys. Rev. A](#) **73**, 013411 (2006).
 - [9] U. Roy, S. Ghosh, P. K. Panigrahi, and D. Vitali, *Sub-planck-scale structures in the pöschl-teller potential and their sensitivity to perturbations*, [Phys. Rev. A](#) **80**, 052115 (2009).
 - [10] S. Choudhury and P. K. Panigrahi, *A proposal to generate entangled compass states with sub-planck structure*, [AIP Conference Proceedings](#) **1384**, 91 (2011).
 - [11] L. Praxmeyer, C.-C. Chen, P. Yang, S.-D. Yang, and R.-K. Lee, *Direct measurement of time-frequency analogs of sub-planck structures*, [Phys. Rev. A](#) **93**, 053835 (2016).
 - [12] M. W. Davis, *The Geometry and Topology of Coxeter Groups. (LMS-32)* (Princeton University Press, 2008).
 - [13] M. Ringbauer, T. J. Weinhold, L. A. Howard, A. G. White, and M. R. Vanner, *Generation of mechanical interference fringes by multi-photon counting*, [New J. Phys.](#) **20**, 053042 (2018).
 - [14] F. Shahandeh and M. Ringbauer, *Optomechanical state reconstruction and nonclassicality verification beyond the resolved-sideband regime*, [arXiv:1709.01135 \[quant-ph\]](#).
 - [15] J. D. Teufel, T. Donner, D. Li, J. W. Harlow, M. S. Allman, K. Cicak, A. J. Sirois, J. D. Whittaker, K. W. Lehnert, and R. W. Simmonds, *Sideband cooling of micromechanical motion to the quantum ground state*, [Nature](#) **475**, 359 EP (2011).
 - [16] H. Miao, K. Srinivasan, and V. Aksyuk, *A microelectromechanically controlled cavity optomechanical sensing system*, [New J. Phys.](#) **14**, 075015 (2012).
 - [17] C. Anastopoulos and B. L. Hu, *Probing a gravitational cat state*, [Classical and Quantum Gravity](#) **32**, 165022 (2015).
 - [18] W. Marshall, C. Simon, R. Penrose, and D. Bouwmeester, *Towards quantum superpositions of a mirror*, [Phys. Rev. Lett.](#) **91**, 130401 (2003).
 - [19] A. Bassi, K. Lochan, S. Satin, T. P. Singh, and H. Ulbricht, *Models of wave-function collapse, underlying theories, and experimental tests*, [Rev. Mod. Phys.](#) **85**, 471 (2013).
 - [20] F. Shahandeh and M. R. Bazrafkan, *General ordering problem and its combinatorial roots*, [J. Phys. A Math. Theor.](#) **45**, 155204 (2012).
 - [21] A. Kenfack and K. Yczkowski, *Negativity of the Wigner function as an indicator of non-classicality*, [J. Opt. B Quantum Semiclassical Opt.](#) **6**, 396 (2004).
 - [22] V. Veitch, N. Wiebe, C. Ferrie, and J. Emerson, *Efficient simulation scheme for a class of quantum optics experiments with non-negative wigner representation*, [New J. Phys.](#) **15**, 013037 (2013).

SUPPLEMENTARY MATERIAL

Theoretical modeling of Wigner functions. To find the Wigner function after applying Eq. 1 to an initial state ρ , we write the final state using symmetric ordering and then make the substitutions $a=1/\sqrt{2}(X+iP)$ and $a^\dagger=1/\sqrt{2}(X-iP)$, where X and P are the position and momentum coordinates in the Wigner function. Before elaborating on this process we rewrite $\Upsilon=e^{-|\alpha|^2}\alpha(e^{i\mu X_M}-e^{i\phi})/\sqrt{2}$ using the displacement operator $\mathcal{D}(\beta,a)=e^{[\beta a^\dagger-\beta^*a]}$ for a displacement by β . To do this we note that $\phi=0$, that $X_M=(1/\sqrt{2})(a^\dagger+a)$; and that overall scalar factors can be ignored as the final state will be normalised. We can then rewrite Υ as;

$$\begin{aligned}\Upsilon &= e^{i\mu X_M} + 1 \\ &= e^{i\mu(1/\sqrt{2})(a^\dagger+a)} + 1 \\ &= e^{(1/\sqrt{2})(i\mu a^\dagger+i\mu a)} + 1 \\ &= \mathcal{D}(i\mu/\sqrt{2}, a) + 1.\end{aligned}\tag{S1}$$

This shows that our measurement operator is equivalent to applying a superposition of the displacement operator and the identity and allows us to use known algebra regarding the displacement operator, e.g., $\mathcal{D}(\alpha, a)|0\rangle=|\alpha\rangle$ and $\mathcal{D}(\alpha, a)=\mathcal{D}^\dagger(-\alpha, a)$.

Writing our initial state ρ using symmetric ordering, $\{e^{-\lambda a^\dagger a}\}_0$ we then need to apply the appropriate number of $\mathcal{D}(i\mu/\sqrt{2}, a)+1$ and $R(\theta)$ operations in Eq. 1, whilst always ensuring that the state is written symmetrically. To calculate the second-order hypercube state we perform the following calculation,

$$\begin{aligned}(\mathcal{D}(-i\mu/\sqrt{2}) + 1)R(\frac{\pi}{2})(\mathcal{D}(-i\mu/\sqrt{2}) + 1)\rho \\ (\mathcal{D}^\dagger(-i\mu/\sqrt{2}) + 1)R^\dagger(\frac{\pi}{2})(\mathcal{D}^\dagger(-i\mu/\sqrt{2}) + 1).\end{aligned}$$

This function has 16 terms. The third- and fourth-order compass states have 64 and 256 terms respectively. An example calculation for one application of the displacement operator to the ground state, i.e., $\mathcal{D}(\beta)\{e^{-\lambda a^\dagger a}\}_0$ using the general ordering theorem developed in Ref. [20] is shown below

$$\begin{aligned}\mathcal{D}(\beta)\{e^{-\lambda a^\dagger a}\}_0 &= e^{(\beta a^\dagger - \beta^* a)}\{e^{-\lambda a^\dagger a}\}_0 \\ &= e^{-|\beta|^2/2}e^{\beta a^\dagger}e^{-\beta^* a}\{e^{-\lambda a^\dagger a}\}_0 \\ &= e^{-|\beta|^2/2}e^{\beta a^\dagger}\{e^{-\beta^* a}e^{-\lambda(a^\dagger - \beta^*/2)a}\}_0 \\ &= e^{-|\beta|^2/2}\{e^{\beta a^\dagger}e^{-\beta^* a}e^{-\lambda(a^\dagger - \beta^*/2)(a - \beta/2)}\}_0\end{aligned}$$

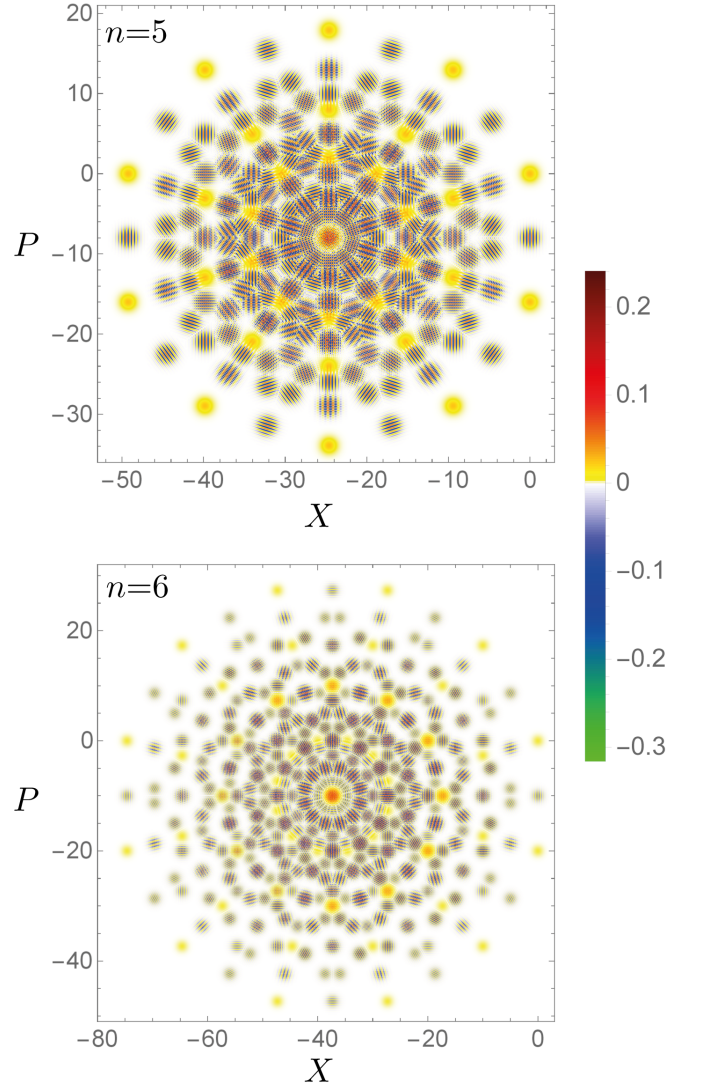


FIG. S1. Density plots of the hypercube state Wigner functions for $n = 5$ and $n = 6$, generated from an initial mechanical ground state respectively for with $\mu = 16$ and 20 . Colour coding as for Fig. 2.

Modelling of experimental uncertainties. A model was constructed to ascertain if our experimental results could be obtained from ideal hypercube states in our experimental regimes by modelling the experimental uncertainties present, namely, drift in the interferometer setting, ϕ ; experimental timing uncertainties when applying $R(\pi/2n)$; and variations from the mean due to counting statistics. The resultant states after accounting for these experimental uncertainties are shown in Fig ?? and show excellent agreement with our measured results.

More detail on the modelling of each experimental uncertainty is now provided. Experimental drift of ϕ between measurements mean that each state preparation is averaged over different values of ϕ . Having recorded the value of ϕ for each measurement, we can compute the range of Υ , average them, and apply the average in Eq. 1. This error was kept small by rejecting datasets

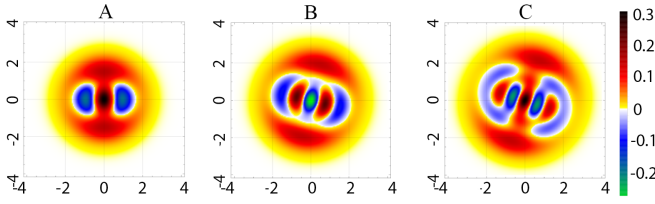


FIG. S2. Theoretical density plots of the Wigner-function for A) second- B) third-, and C) fourth-order hypercube states for $\bar{n}=0$ and $\mu=8\times 10^{-9}$ in units of the ground state width. Each state exhibits a minimum Wigner negativity of ≤ -0.2 . The rotations observed in B) and C) are due to additional phases acquired from multiple applications of the displacement operator.

with drifts larger than 10° . Timing Uncertainty between photon detections of ± 15 ns resulted in uncertainty in the argument of rotation operator $R(\pi/2n)$ in Eq. 1. This timing uncertainty, δt , was approximated by averaging two states with $R(\pi/2n + \delta t\pi/T)$ and $R(\pi/2n - \delta t\pi/T)$. Finally, a normalised probability density plot from a number of samples (equal to that in the experiment) from this distribution, taking into account Poissonian counting statistics.

Multiple displacements. Multiple applications of the displacement operator break the symmetry of our protocol, by applying a phase to the bottom fringe—the lowest in phase quadrature—see e.g. the middle panels in the top row in Fig. 2. To see this, note that the initial state at the origin of phase space is first displaced in the negative X and then in the negative P direction in Fig. 2. Consequently, the top and side fringes originate from a single application of the displacement operator, while the bottom fringes are the result of two applications, which acquire an additional phase due to the relation $\mathcal{D}(\alpha)\mathcal{D}(\beta)=e^{\frac{1}{2}(\alpha\beta^*-\alpha^*\beta)}\mathcal{D}(\alpha+\beta)$. This phase change becomes more obvious as the fringe wavelength increases with decreasing separation between the coherent states. Figure S2 shows how this effect results in a rotation for higher order hypercube states in the regime of vanishing coupling strength.

Alternative quantitative indicators for sensing. We outline the use of the Wigner negativity to quantify the sensitivity of hypercube states to small displacements.

The volume of Wigner negativity is a commonly used measure of the quantumness of a state [21] and has operational significance as a necessary condition for computation work [22]. In Fig. S4 we calculate the volume of Wigner negativity for the second-, third- and fourth- order hypercube states for the conditions of each row from Fig. 4. We see that for large coupling, the Wigner negativity increases significantly with the order of the state (top row) and persists for large $\bar{n}=10$ (bottom row). Even for small coupling, $\mu=8\times 10^{-9}$,

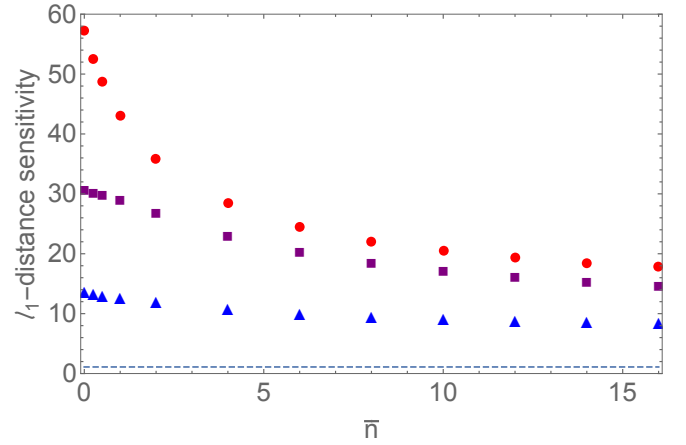


FIG. S3. ($\mu=12$; $\bar{n}=0 \rightarrow \bar{n}=15$). Sensitivity for displacements in momentum (or equally position) for second- (blue triangles), third- (magenta squares) and fourth- (red dots) order hypercube states. Hypercube states are more sensitive than even zero-temperature coherent states for a wide range of experimental parameters; note the increase in sensitivity with the order of the hypercube state.

the negativity is evident for temperatures $\bar{n}<2$ (middle row). Figure S2 highlights that even in this cold small coupling limit Wigner negativity is a prominent feature of hypercube states.

Experimental details & data analysis. The mechanical resonator used in our experiment is a high stress 1.7×1.7 mm Si_3N_4 membrane encased in a 10×10 mm silicon frame. The membrane has a thickness of 50 ± 2.5 nm and a reflectivity of $23\pm 0.5\%$, at a wavelength of 795 nm. At the same wavelength the frame has a reflectivity of $20.5\pm 0.2\%$. The resonance frequency of the membrane is 105.64kHz, with the FWHM of the noise-power spectrum being 3.1 ± 0.05 kHz. The membrane was driven using a Steminac SM412 ring-piezo which has a nominal resonance frequency of 1.7 MHz and an operating capacitance of 1.8 nF.

Photon detection signals from the avalanche photodiode are split, delayed and fed into a time-tagging coincidence logic. Upon finding the requisite coincidence event the logic triggers an oscilloscope which records a trace of the homodyne signal measuring the membranes position. This trace consists of 2500 points sampled at a rate of 100MS/s resulting in a $25\mu s$ window around the trigger event. The X -, P - and ϕ - values for each trace were obtained from a fit of the mechanical response function and the phase space distribution was reconstructed from all fits. The function used for the fitting was,

$$1 - d \left| \cos \left[\omega_M t + \arctan(X/P) - \frac{\pi}{4} \right] \right| \quad (S2) \\ \times A \cos \left[(X \cos(\omega_M t) + P \sin(\omega_M t) + \phi) + c \right]$$

where A is the amplitude of the homodyne signal, ω_M is the resonance frequency of the mechanical resonator, ϕ is

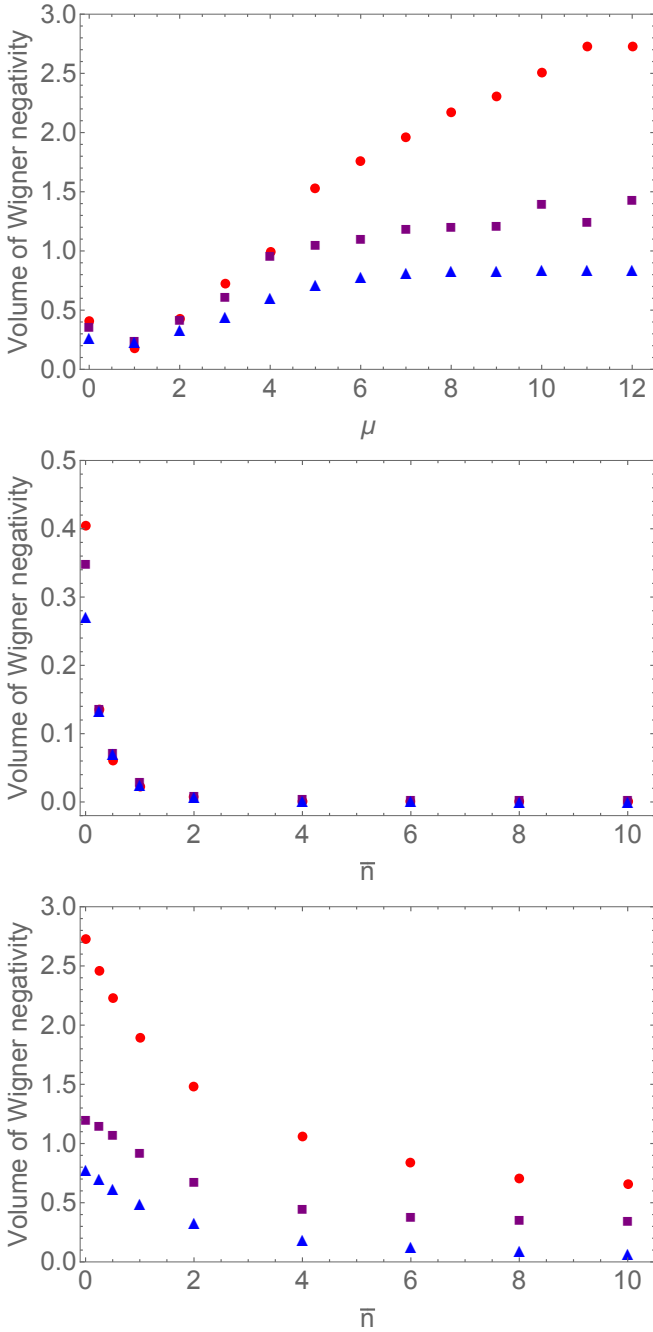


FIG. S4. Volume of Wigner negativity for second- (blue triangles), third- (purple squares) and fourth-order (red circles) hypercube states. **Top Row.** Cold temperature: large \rightarrow small coupling ($\bar{n}=0$; $\mu=6 \rightarrow \mu=8 \times 10^{-9}$). **Middle Row** Small coupling: cold \rightarrow hot temperature ($\mu=8 \times 10^{-9}$; $\bar{n}=0 \rightarrow \bar{n}=10^{15}$; the colours in the last panel are scaled by 10^8 in accordance with the axis scaling). **Bottom Row** Large coupling: cold \rightarrow warm temperature ($\mu=6$; $\bar{n}=0 \rightarrow \bar{n}=6$).

the static phase shift along the arm of the interferometer incident on the membrane frame, c is the DC-component in the signal due to the loss along each arm of the interferometer being asymmetric and d describes the strength of the membrane amplitude modulation that occurs at

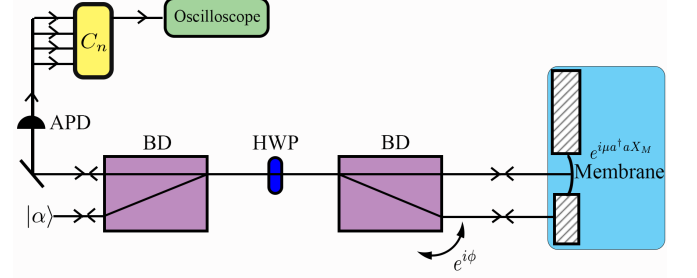


FIG. S5. A weak coherent state $|\alpha\rangle$ is inserted and split using a half wave plate (HWP) and a beam displacer (BD) into two arms of a folded interferometric setup, see Ref. [13] for details. The optical field in the top arm interacts with a membrane mechanical resonator via radiation pressure, described by $e^{i\mu a^\dagger a X_M}$. Here a and a^\dagger are the annihilation and creation operators, μ is the optomechanical coupling strength and X_M is the mechanical position operator. The bottom arm interacts with the static frame of the membrane, obtaining a controllable phase shift $e^{i\phi}$, which we set to $\phi = \pi$. Post these interactions, the optical fields in both arms are interfered, split into the polarisation components and detected in an avalanche photon detector (APD). The detector signal is then split into two, three or four paths depending on whether detection of a second, third or fourth order hypercube is being made; with each path past the first adding a time delay of $T/2n$. Coincidence counting between the paths is made at C_n , and upon detection of a coincidence event an oscilloscope is triggered to record a trace of the membrane's position from the back (not shown).

larger amplitudes. The phase space readout used a balanced photodetector with a gain of 10^5 V/A and a bandwidth of 4 MHz. The DC component c was compensated to zero by adding an adjustable loss element in front of one detector. Since ω_M , A , c , d were measured independently and constant during measurement, and the other variables, namely, X , P and ϕ , all could be used to find unique, repeatable and accurate fits to the signal.